Journal of Power Sources 439 (2019) 227026

Contents lists available at ScienceDirect

Journal of Power Sources

journal homepage: www.elsevier.com/locate/jpowsour

Oxygen-defective Co_3O_4 for pseudo-capacitive lithium storage

Jie Zhang [a], Heng Jiang [b], Yibo Zeng [a], Ying Zhang [c], Hang Guo [a,*]

[a] Pen-Tung Sah Institute of Micro-Nano Science and Technology, Xiamen University, 361005, Xiamen, People's Republic of China
[b] College of Materials, Xiamen University, 361005, Xiamen, People's Republic of China
[c] Xiamen University Malaysia, 43900, Sepang, Selangor Darul Ehsan, Malaysia

HIGHLIGHTS

- Oxygen-defective Co_3O_4 anode was prepared via a facile coordination strategy.
- Phase and morphology evolution of Co_3O_4 were revealed by ex-situ characterization.
- Lithium storage in Co_3O_4 is dominated by a pseudo-capacitance controlled process.

ARTICLE INFO

Keywords:
Oxygen vacancy
Transiton metal oxide
Lithium ion batteries

ABSTRACT

Transition metal oxide is widely studied type of high-capacity anode material for lithium ion batteries. Herein, oxygen-defective cobalt oxide with attractive lithium storage performance is prepared via a two-step strategy. Experimental results shows that there is certain amount of oxygen vacancies in Co_3O_4. Reversible conversion between metallic Co and CoO during the charge-discharge process was revealed by ex-situ XRD. Reversible morphology evolution is also confirmed by the ex-situ FE-SEM. The oxygen-defective Co_3O_4 anode shows attractive stability and rate performance. It possesses a discharge capacity of 1006 mAh·g^{-1} in the first cycle, with a high initial Coulombic efficiency of 73.9%. A reversible capacity of 896 mAh·g^{-1} can be maintained after 200 cycles at 250 mA g^{-1}. It could even stably operate at an elevated current density of 5000 mA g^{-1} for 500 times. Further kinetic analysis reveals that pseudo-capacitance plays a dominant role in the lithium storage of oxygen-defective Co_3O_4. Existence of oxygen vacancies could not only facilitate Li^+ migration but also enhance electric conductivity to a certain extent, resulting in improved lithium storage performance.

1. Introduction

The increasing popularity of mobile electrical devices and hybrid electric vehicles in recent years has greatly spurred record-breaking innovations in energy conversion storage technology. As the most popular energy storage device, lithium ion battery (LIB) has constantly been a research hotspot in the previous several decades. Although LIBs possess a series of advantages such as attractive cycling stability and operating safety, challenges still do exist. For example, energy density of LIBs using graphite as anode is going to reach its ceiling [1–3]. In addition, the power density of LIBs is far from satisfying as well. Thus, improvement in energy density and power density of LIBs is urgently needed [4]. Although metallic lithium (Li) anode has recently captured a lot attention, the related research is still in its infancy stage. Due to ultra-high theoretical lithium storage capacity, alloying-type anodes such as silicon (Si), tin oxide (SnO_2) and their derivatives have also aroused enormous interest. The huge volume expansion ratio, however, is an inevitable challenge, which would seriously hinder the cycling stability [5]. Although some strategies such as carbon coating, designing hollow structures have been put forward to overcome the above issue. Generally, this objective could only be realized at the expense of relative complicated procedures and low volume energy density [6–10].

Recently, some researcher have shifted their focus on conversion reaction anodes, which have moderate capacity and volume expansion ratio [11–13]. Due to reversible conversion between zero oxidation state metallic atom and higher oxidation state metal oxide, conversion mechanism anodes have higher lithium storage capacity than intercalation anodes. In addition, the volume expansion ratio of conversion anodes is generally smaller than that of alloying anodes. As a typical kind of conversion anode, transition metal oxides (TMOs) have captured much attention due to low cost and attractive electrochemical properties [14]. Among various TMO anodes, cubic nickel oxide (NiO) and spinel

* Corresponding author.
E-mail address: hangguo@xmu.edu.cn (H. Guo).

https://doi.org/10.1016/j.jpowsour.2019.227026
Received 22 February 2019; Received in revised form 27 June 2019; Accepted 16 August 2019
Available online 4 September 2019

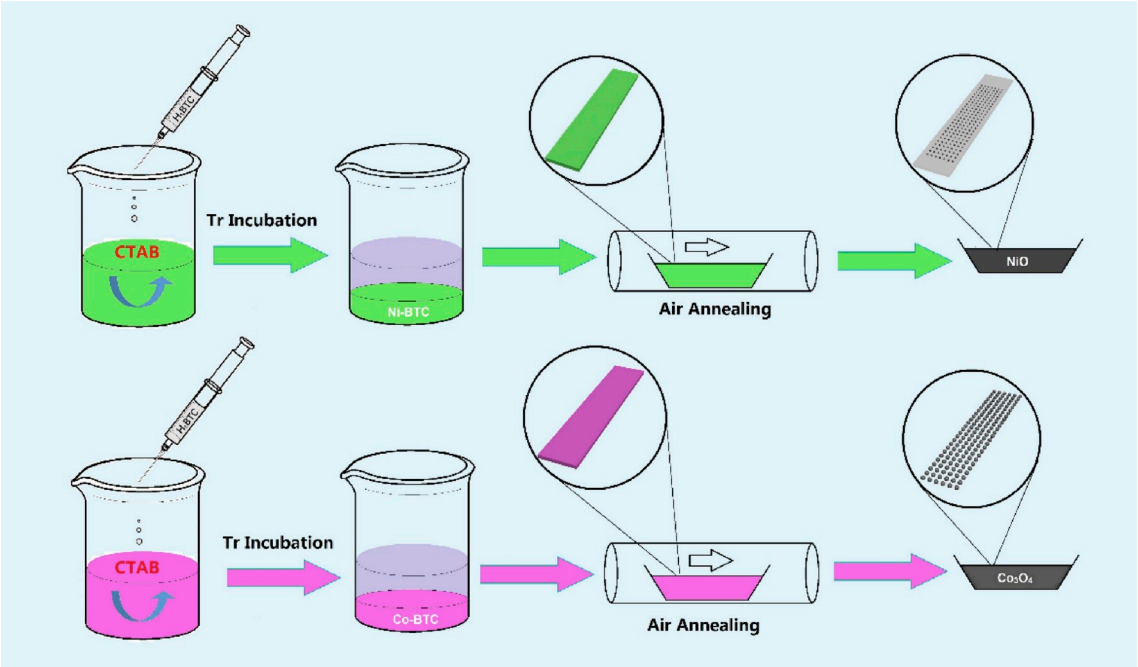

Fig. 1. Schematic illustration for preparation of NiO and Co_3O_4 nanosheets.

cobalt oxide (Co_3O_4) have been widely studied. Theoretical lithium storage capacity of cubic NiO and spinel Co_3O_4 is 718 and 890 mAh g^{-1}, which is much higher than that of graphite anode [15,16]. Although NiO and Co_3O_4 have attractive lithium storage capacities, their volume expansion could not go unnoticed. In order to alleviate the issue mentioned above, various micro/nanostructures of NiO have been designed. Nanostructured NiO such as nanoparticle [16–19], nanosheets [20–23], nano octahedrons [24] and hollow spheres [25–31] prepared by different methods showed attractive electrochemical performance. For example, the hollow NiO octahedrons prepared through Kirkendall effect by the Park group could have a high reversible capacity of 1234 mAh g^{-1} at 1000 mA g^{-1} after 150 cycles [24]. These yolk-shell NiO microspheres modified by graphene quantum dots showed superior performance. It could stably cycle for 250 times at 100 mA g^{-1} with a capacity of 1081 mAh g^{-1} [28]. A range of Co_3O_4 structures such as nanowires [32,33], nanoparticles [34–38], nanosheets [39–43], nanotubes [44–46], hollow dodecahedra [47–49] and hollow spheres [50–53] have also been prepared via various methods. The Zhen group fabricated Co_3O_4 nanotube anode via a template-free strategy. Multifunctional Co_3O_4 nanotube could stably cycle for 50 times at 100 mA g^{-1} with a capacity of 1081 mAh g^{-1} [44]. Selecting ZIF-67 as precursor, the Mai group prepared yolk-shell Co_3O_4/C composites with outstanding lithium and sodium storage capacity [49]. The composite anode could retain a reversible capacity of 1100 mAh g^{-1} at 200 mA g^{-1} after 120 cycles. All these examples demonstrated that NiO and Co_3O_4 could be used as promising anode materials for high performance LIBs.

Metal organic frameworks (MOFs) and their derivatives are two important families of functional energy storage and conversion materials. Their high porosity, versatile functionalities, controllable chemical compositions and diverse structures offer immense possibilities in the search for adequate electrode materials for rechargeable batteries [54]. The Kim group reported preparation of NiO nanoparticle via the combustion of MOF precursor [15]. The Li group fabricated a unique flower-like Co_3O_4/C hybrid using novel cobalt-based MOFs as precursor [38]. The MOF-derived anode possesses a capacity of 671 mAh g^{-1} at a high current density of 1000 mA g^{-1}.

Herein, MOF-derived Co_3O_4 with certain amount of oxygen vacancies was prepared via a two-step strategy. The as-prepared oxygen-defective Co_3O_4 anode showed attractive electrochemical performance. In addition, pseudo-capacitance was found to make a major contribution to the overall lithium storage capacity. The oxygen-defective Co_3O_4 demonstrated as a promising anode for high performance LIBs.

2. Experimental section

2.1. Preparation of oxygen-defective NiO and Co_3O_4

The oxygen-defective NiO and Co_3O_4 were prepared via an initial room temperature incubation and a subsequent thermal treatment in air atmosphere. Typically, 10 mmol nickel acetate ($Ni(Ac)_2 \cdot 4H_2O$) and 2.0 g hexadecyl trimethyl ammonium bromide (CTAB) was sequently dissolved in a 60 mL mixed solution of deionized water and ethanol absolute (DI H_2O:Eth = 1:1 *v:v*). Then, a 60 mL mixture of DI H_2O and Eth (*v:v* = 1:1) containing 2.0 g trimesic acid (H_3BTC) was dropwise added into the above solution under magnetic stirring. Light green floc was obtained after a 15-min stirring. The mixture was then incubated at room temperature for 24 h. After repeated rinse with DI H_2O and ethanol, a light green filter cake was obtained. The intermediate was then vacuum dried at 60 °C for 12 h before thermal treatment. Loading in a ceramic boat, the NiO intermediate was annealed at 350 °C for 2 h in air, with a ramping rate of 1 °C min^{-1}. The light green color turned into black after annealing. The as-obtained sample was labeled as NiO. And Co_3O_4 was prepared via a similar procedure, in which $Ni(Ac)_2$ was replaced with cobalt acetate ($Co(Ac)_2$). These final products were grinded into powder for further test and characterization.

2.2. Characterization

X-ray diffraction (XRD) patterns were collected on a Rigaku Ultima IV Diffractometer with a Cu Kα source. Scanning electronic microscope (SEM) images were obtained on a Carl ZEISS SUPRA 55 microscope. Transmission electron microscopy (TEM), high resolution transmission electronic microscope (HR-TEM) images and element mapping were measured on FEI Talaos F200S equipped with an energy dispersive X-ray spectrum (EDS) analyzer. X-ray photoelectron spectroscopy (XPS) were tested with a PHI-1600 spectrometer with Al Ka radiation. All binding energies were referenced to C1s peak at 284.8 eV.

The content of oxygen vacancies (δ) was measured by the iodimetry

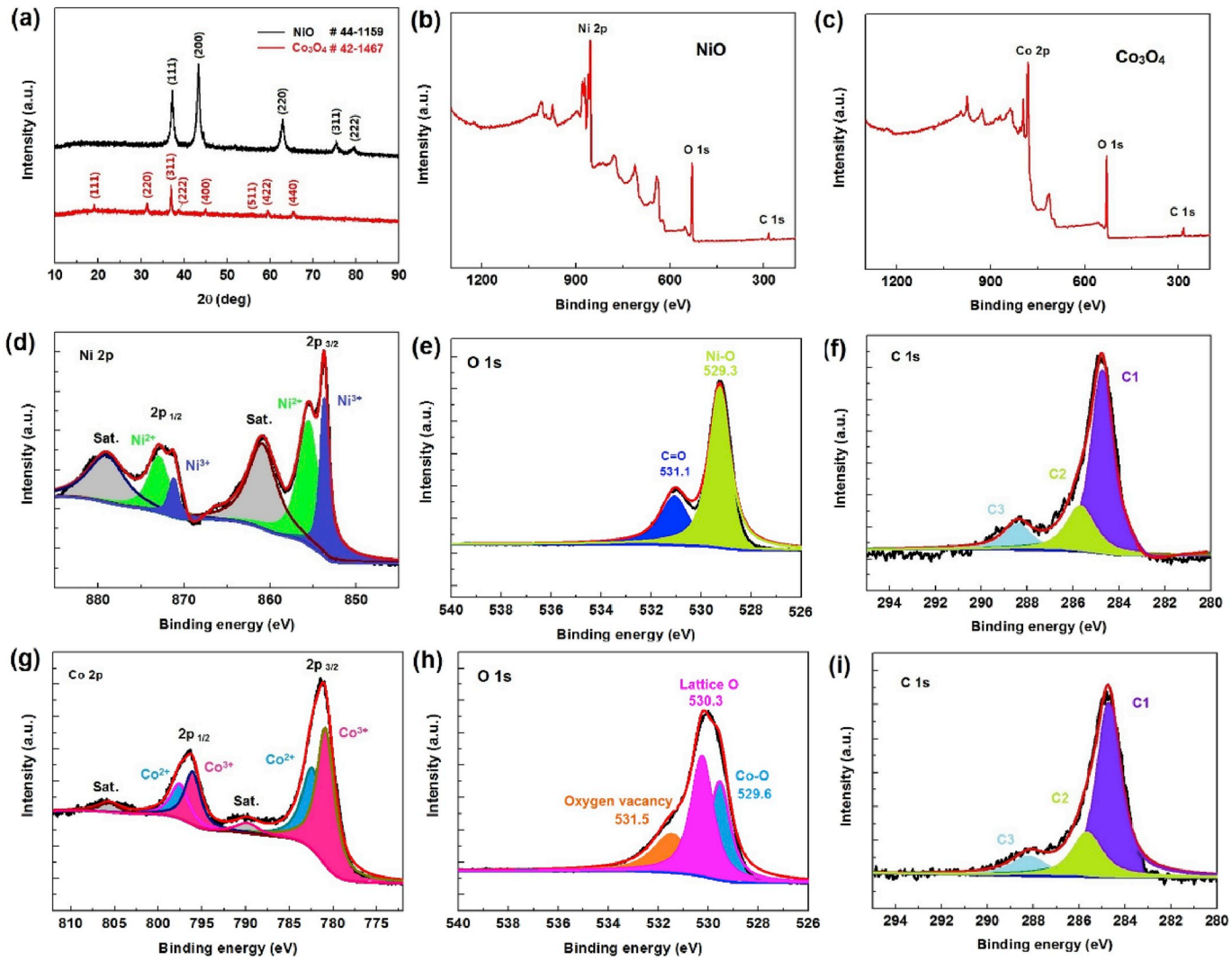

Fig. 2. Characterizations of NiO and Co_3O_4 by XRD and XPS. (a) XRD patterns of NiO and Co_3O_4; (b) Survey spectrum of NiO; (c) Survey spectrum of Co_3O_4 (d)–(f) XPS spectra of NiO; (g)–(i) XPS spectra of Co_3O_4.

based oxidation-reduction titrations. In a typical process, an accurately weighed sample in a 250 mL conical flask was dispersed in 10 mL of KI aqueous solution (70 mg mL^{-1}) under the protection of N_2 atmosphere. Then 7 mL of HCl solution (6 mol L^{-1}) and 50 mL of H_2O was added to the dispersion. A starch indicator and a $Na_2S_2O_3$ solution with calibration concentration (C) were used to titrate the mixture above. The oxygen vacancies (δ) could be calculated according to the following equations.

$$Co_3O_{4-\delta} + (8-2\delta)H^+ + (2-2\delta)I^- \rightarrow 3Co^{2+} + (4-\delta)H_2O + (1-\delta)I_2 \quad (1)$$

$$(1-\delta)I_2 + (2-2\delta)S_2O_3^{2-} \rightarrow (1-\delta)S_4O_6^{2-} + (2-2\delta)I^- \quad (2)$$

Thus, the molar ratio (n) of $Co_3O_{4-\delta}$ and $S_2O_3^{2-}$ could be calculated as

$$n(Co_3O_{4-\delta}):n(S_2O_3^{2-}) = 1:(2-2\delta) \quad (3)$$

That is, m:$(240.8–16\delta) = CV/(2-2\delta)$ (4)

where, m is the mass of as-measured sample, C is the concentration of $Na_2S_2O_3$ solution, V is the volume of $Na_2S_2O_3$ consumed in the titration.

2.3. Electrochemical measurements

The NiO and Co_3O_4 were ball-milled into slurry with Super P and poly-vinylidene fluoride (PVDF) powder using N-methyl-2-pyrrolidone (NMP) as solvent. The mass ratio of active species, conductive agent and binder was 6:2:2. The slurry was then coated on copper (Cu) foil with a thickness of 50 μm by a thin film applicator. Slurry-coated Cu foil was vacuum dried at 60 °C for 12 h and cut into circular discs with a diameter of 1.6 cm CR2016 coin cells were assembled in an argon filled glove box, with metallic lithium foil as counter electrode and Celgard 2500 polypropylene membrane as the separator. Lithium hexafluorophosphate solution ($LiPF_6$, 1.0 mol L^{-1}) in a mixture of ethylene carbonate, dimethyl carbonate, and ethyl methyl carbonate (EC, DMC, EMC $v/v/v = 1:1:1$) was used as the electrolyte. Galvanostatic discharge-charge (GDC) and long-term cycling stability test were performed on Neware battery test system within a potential range from 0.01 to 3.0 V (vs. Li/Li^+). Cyclic voltammetry (CV) and electrochemical impedance spectroscopy (AC-EIS) measurement were carried out on a CHI660E electrochemical workstation. AC-EIS curves was measured with a 10 mV voltage amplitude in a frequency range of 0.01 Hz–100 kHz.

3. Results and discussion

As illustrated in Fig. 1, NiO and Co_3O_4 nanosheets were prepared via a two-step procedure. In the first step, transition metal ions (Ni^{2+}, Co^{2+}) were evenly dispersed in a mixed solvent in the existence of CTAB as surfactant. Addition of H_3BTC would trigger an immediate coordinative reaction between metal ions and organic ligand. Under the assistance of

Table 1
Oxygen vacancies (δ) in as-prepared samples.

Sample	m (g)	C (mol L^{-1})	V (mL)	δ
NiO	0.0508	0.02	20.3	0.025
Co_3O_4	0.0512	0.02	16	0.243

constant stirring, these ligand units were evenly coordinated with metal ions. After a 24-h incubation at room temperature, coordinative intermediates were obtained. Subsequent thermal treatment in air atmosphere would initiate the thermal decomposition of transition metal-organic ligand coordinative intermediates. With the conversion of organic component into gaseous carbon oxide and dehydration of MOF intermediates, the Ni-BTC and Co-BTC were converted into NiO and Co_3O_4, respectively.

XRD and XPS characterization were applied to determine the component of these as-prepared samples. The corresponding XRD patterns and XPS spectra were presented in Fig. 2.

As revealed in Fig. 2a, both the NiO and Co_3O_4 showed their own distinct characteristic diffraction peaks in the scanning range. A series of peaks were observed at 37.4, 43.4, 63.2, 75.3 and 79.8° in the XRD pattern of NiO, corresponding to the (111), (200), (220), (311) and (222) planes of cubic NiO (JCPDS NO. 44-1159). The Co_3O_4 showed a series of peaks well-fitted with the (111), (220), (311), (222), (400), (422), (511) and (440) planes of cubic spinel Co_3O_4 (JCPDS NO. 42-1467). Thus, these final samples were determined as NiO and Co_3O_4 according to analysis of XRD patterns. Further component analysis of NiO and Co_3O_4 was accomplished by XPS. As displayed in Fig. 2b and c, signals of Ni, O, C elements and Co, O, C elements were detected in survey spectra of NiO and Co_3O_4, respectively. For the Ni 2p peaks in

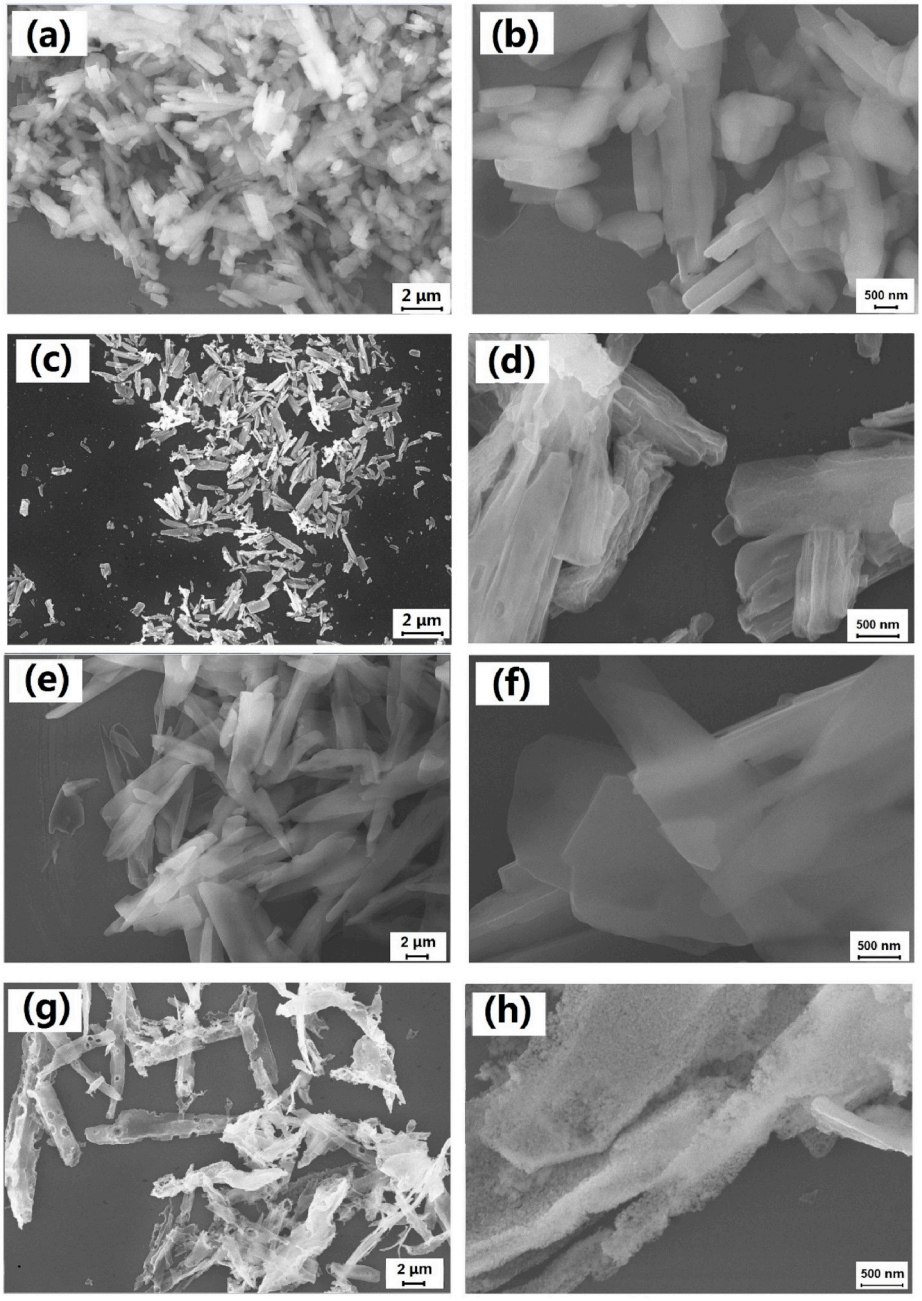

Fig. 3. FE-SEM images of transition metal-BTC intermediate and their derived metal oxide. (a)–(b) NiO intermediate; (c)–(d) NiO; (e)–(f) Co_3O_4 intermediate; (g)–(h) Co_3O_4.

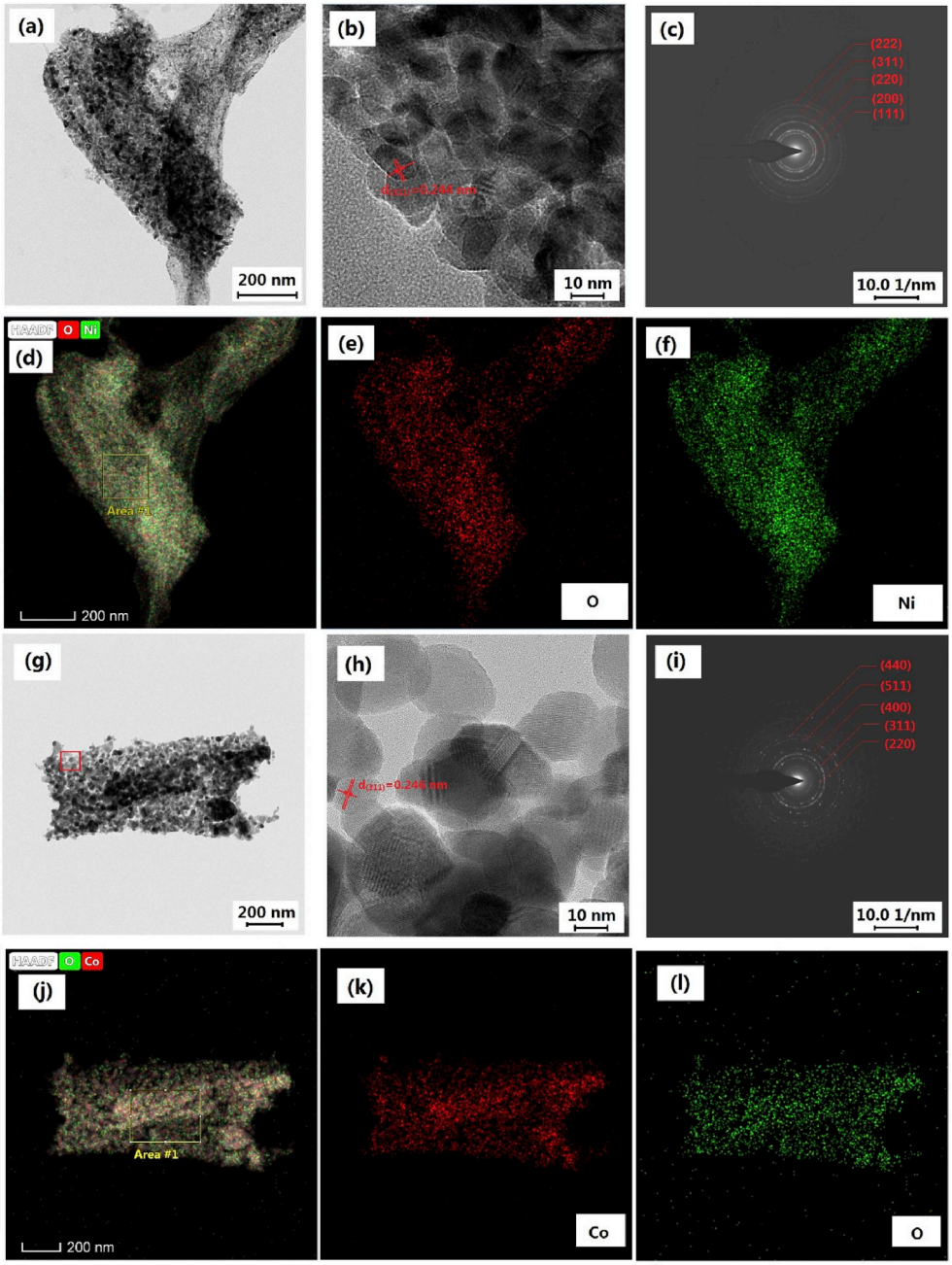

Fig. 4. TEM, SAED and EDS mapping images of the as-prepared samples. (a)–(b) TEM image of NiO; (c) SAED pattern of NiO; (d)–(f) EDS mapping images of NiO; (g)–(h) TEM image of Co_3O_4; (i) SAED pattern of Co_3O_4; (j)–(l) EDS mapping images of NiO.

NiO, peaks at 855.5eV (Ni $2p_{3/2}$) and 873.8 eV (Ni $2p_{1/2}$) were related to Ni^{2+}, peaks at 853.3 eV (Ni $2p_{3/2}$) and 870.7 eV (Ni $2p_{1/2}$) were related to Ni^{3+}. Energy separation between the Ni $2p_{1/2}$ and Ni $2p_{3/2}$ peak was measured to be 20.3 eV. The O 1s peaks of NiO shown in Fig. 2e consists of an intense peak and an obvious shoulder peak. Further fitting revealed that the O 1s spectrum could actually be splitted into a pair of peaks. Peak at 529.3 and 531.1 eV is related to the Ni–O bond (lattice oxygen reconstructed), and C═O interaction, respectively [24]. The C 1s profile can be splitted into three peaks at 284.6, 285.8 and 288.1 eV, which could be attributed to graphite-like carbon (C–C), C–OH bond and C═O bond, respectively [15]. The Co 2p profile of Co_3O_4 was shown in Fig. 2g, peaks at 781.4 eV (Co $2p_{3/2}$) and 797.9 eV (Co $2p_{1/2}$) are related to Co^{2+}, peaks at 779.3 eV (Co $2p_{3/2}$) and 796.5 eV (Co $2p_{1/2}$) are related Co^{3+} [55]. Energy separation between Co $2p_{1/2}$ and Co $2p_{3/2}$ was measured to be about 15.1 eV. The O 1s profile in Co_3O_4 is obviously different from that in NiO, with a weaker shoulder peak at around 531.5 eV, which is ascribed to defects with low oxygen coordination (oxygen vacancy). The other two peaks at 529.6 and 530.3 eV can be ascribed to lattice oxygen (Co–O bond) [56]. The appearance of XPS peak at 531.5 eV indicates the existence of oxygen vacancy in Co_3O_4. The C 1s profile of Co_3O_4 shows no obvious difference from that of NiO. The XPS spectra analysis indicated both NiO and Co_3O_4 have certain amount of oxygen vacancies in their structure. And the Co_3O_4 might have a higher oxygen vacancy density than the NiO. Previous reports have confirmed that oxygen vacancies in metal oxides is beneficial to the electrochemical performance [60]. Introduction of oxygen vacancies would break charge equilibrium, resulting in formation of a local bulit-in electric field. This electric field would alter the charge transfer pathway, facilitating lithium ions (Li^+) diffusion and electron transfer in electrode [68]. Thus, oxygen-defective NiO and Co_3O_4 could be used as

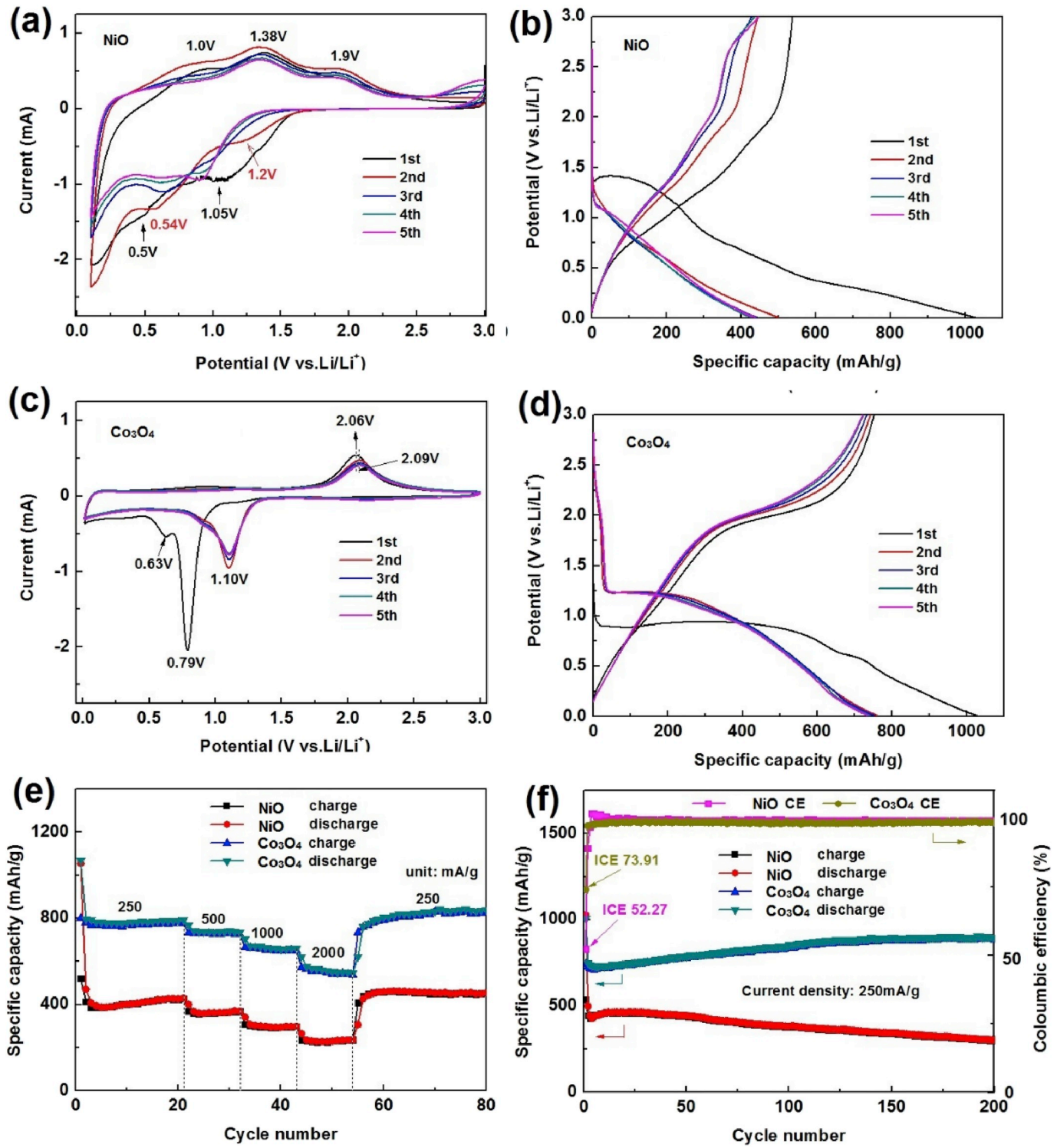

Fig. 5. Electrochemical performance tests of NiO and Co_3O_4 anode. (a) CV curves of NiO at a scan rate of 0.25 mV s^{-1}; (b) GCD curve of NiO at a current density of 250 mA g^{-1}; (c) CV curves of Co_3O_4 at a scan rate of 0.25 mV s^{-1}; (d) GCD curve of Co_3O_4 at a current density of 250 mA g^{-1}; (e) Rate capabilities of NiO and Co_3O_4; (f) 200-cycle GCD test curves of NiO and Co_3O_4 anode at a low current density of 250 mA g^{-1}.

promising anode materials for LIBs.

In order to quantitatively study the relative content of oxygen vacancies, the oxygen non-stoichiometry was measured by iodometry at 25 °C [57]. Detailed oxygen vacancies (δ) of the NiO and Co_3O_4 was summarized in Table 1, where NiO has a much lower oxygen vacancy content than Co_3O_4.

Morphology feature of MOF intermediates and their derived metal oxides were revealed by FE-SEM. Fig. 3 shows typical morphology of Ni-BTC, NiO, Co-BTC and Co_3O_4. As revealed in Fig. 3a–b, Ni-BTC shows rod-like morphology with smooth surface. Average width of these rods was measured to be about 250 nm. Some obvious changes in morphology could be observed after thermal treatment in air atmosphere (See Fig. 3c–d). Surface roughness of NiO is found to be larger than the Ni-BTC, as some wrinkles could be found on the surface of NiO.

The Co-BTC shows a similar rod-like morphology to that of the Ni-BTC. The average width of Co-BTC, however, is much larger than Ni-BTC. More pronounced change in morphology occurred during the thermal treatment of Co-BTC. Surface roughness of Co_3O_4 is obviously higher than that of NiO, as some irregular-shaped pores could be found on the Co_3O_4 surface. Formation of these pores may result from release of gases generated by combustion of organic component during the annealing process. Sheet-like Co_3O_4 was found to be constructed by large amount of nanoparticles.

A more detailed structural investigation of NiO and Co_3O_4 was realized by TEM. As shown in Fig. 4a, NiO nanosheets is constructed by numerous nanoparticles. Adjacent subunits were densely stacked, forming an interconnected network. The HR-TEM image shown in Fig. 4b revealed these nanoparticles have an average diameter about 20 nm. Inter-planar distance of NiO was measured to be about 0.244 nm, corresponding to the (311) plane of cubic NiO. Coaxial diffraction rings indicated NiO is polycrystalline in nature. From the core to outer shell shown in Fig. 4c, diffraction rings corresponding to (111), (200), (220), (311) and (222) plane of cubic NiO could be observed. EDS mapping images revealed Ni and Co element were evenly distributed in the NiO. It is universally accepted that uniform component distribution is beneficial to cycling stability due to identical expansion coefficient [58]. The Co_3O_4 nanosheet is made up of nanoparticle units as well. Pore size between adjacent units is found to be larger than that in NiO. Average distance between adjacent plane is measured to be 0.246 nm, corresponding to the (311) plane of cubic spinel Co_3O_4. The Co_3O_4 is also polycrystalline, as diffraction rings related to (220), (311), (400), (411) and (440) plane of cubic Co_3O_4 could be detected in SAED patterns. Uniformly distributed Co and O elements indicated the Co_3O_4 has a homogeneous composition, which enables Co_3O_4 to be a stable electrode material. Detailed element content reports shown in Fig. S1 also confirmed existence of oxygen vacancies in NiO and Co_3O_4.

Electrochemical performance of NiO and Co_3O_4 were investigated by CV test and GCD test in a potential range from 0.01 to 3.0 V. Fig. 5a shows CV curves of the NiO at a scan rate of 0.25 mV s^{-1}. A pair of reduction peaks at 1.05 and 0.5 V were observed in the first cathodic scan, which could be attributed to reduction of NiO to metallic Ni and formation of solid electrolyte interphase (SEI) film [18]. There are three peaks at 1.0, 1.38 and 1.9 V related to oxidation of Ni^0 to NiO in the first anodic scan. In the following scans, reduction peaks shifted to higher potentials while oxidation peaks remained unchanged. As shown in Fig. 5b, GCD curves of NiO were featured with clear slopes, which indicated the existence of polarization in electrode material [58]. Initial CV and GCD curves did not overlap well, which means NiO electrode had not get stabilized yet. The Co_3O_4 showed more pronounced redox peaks and charge-discharge plateaus. A strong peak and a weaker shoulder peak could be observed in the first cathodic scan. The main peak at 0.79 V is acsribed to the reduction of Co_3O_4 to metallic Co, and the shoulder peak at 0.63 V is related to the formation of SEI. The strong peak at 2.06 V during the first anodic scan is attributed to oxidation of metallic Co to CoO [35]. Reduction peak shifted to 1.10 V in following scans, which is generally interpreted as reduction of CoO to metallic Co [59–64]. The redox peaks of Co_3O_4 kept unchanged in following scans, indicating good cycling stability. Compared with NiO, the Co_3O_4 shows more pronounced charge/discharge plateaus in the test potential range. In order to compare the rate performance of NiO and Co_3O_4, both anodes were tested under various current densities ranging from 250 to 2000 mA g^{-1}. As shown in Fig. 5e, Co_3O_4 showed obviously higher rate performance than NiO. Average reversible capacity of the Co_3O_4 at 250, 500, 1000 and 2000 mA g^{-1} is calculated to be 783, 735, 660 and 556 mAh g^{-1}, respectively. Corresponding rate capacity of NiO is 405, 360, 293, 227 mAh g^{-1}, which is much lower than Co_3O_4. Attractive rate performance of Co_3O_4 could be attributed to these following reasons. (1) Co_3O_4 has a higher intrinsic electrical conductivity than NiO; (2) Co_3O_4 possesses a higher oxygen vacancy density than NiO, which enables Co3O4 enhanced charge transfer. Initial specific discharge and charge capacity of Co_3O_4 and NiO is 1006-744 and 1027-537 mA h g^{-1} at 250 mA g^{-1} (See Fig. 5f). Initial coulombic efficiency (ICE) of Co_3O_4 and NiO is calculated to be 73.91% and 52.27%, respectively. Irreversible capacity loss (ICL) in the first cycle is believed to originate from the formation of SEI film, during which some of Li^+ions would be irreversibly consumed [46]. Both Co_3O_4 and NiO showed initial discharge capacity slightly higher than their theoretical value, which may result from extra lithium storage at oxygen vacancy sites [60]. After a 200-cycle GCD test at 250 mA g^{-1}, Co3O4 could still maintain a high capacity of 896 mAh g^{-1}. The NiO anode showed inferior stability than Co_3O_4, only a reversible capacity of 303 mAh g^{-1} could be remained.

A further comparison of cycling stability was conducted by testing the NiO and Co_3O_4 anodes at higher current densities (See Fig. S2). Both NiO and Co_3O_4 anodes were pre-tested at a current density of 250 mA g^{-1} for 20 cycles before cycling test. As shown in Fig. S2a, the Co_3O_4 anode could reversibly deliver a discharge capacity of 453 mAh g^{-1} at 2000 mA g^{-1} after 200 cycles. The corresponding capacity retention of Co_3O_4 is calculated to be 80.7%. Reversible capacity of the NiO anode gradually decreased from 294 to 219 mAh g^{-1}, with a relative low capacity retention of 74.5%. With the increase of current density, capacity retention of the electrode would decrease accordingly [43]. The Co_3O_4 anode could maintain a capacity of 250 mAh g^{-1} at a high current density of 5 A g^{-1}, with a capacity retention of 68.1%. With a lower pristine value of 199 mAh g^{-1}, reversible capacity of NiO gradually went down to 123 mAh g^{-1} after 500 cycles. Obviously, the Co_3O_4 has higher cycling stability than the NiO anode. Performance comparison tables were presented in Tab S1–S2.

In order to clarify the Li^+ ions storage kinetic of these as-prepared anodes, CV curves of NiO and Co_3O_4 were collected at various scan rates. Fig. S3a shows the CV curves of NiO at different scan rates from 0.25 to 1.50 mV s^{-1}. As the gradual increase of scan rate, the main reduction peak shifted to lower potential while the main oxidation peak moved toward the opposite direction. The CV curves of Co_3O_4 showed similar trend to the NiO upon the variation on current density (See Fig. S3d).

Based on the assumption that current (i) obeys a power-law relationship with scan rate (v), as shown in Eq (1) [49].

$$i = av^b \tag{5}$$

where a is a constant. b value could be obtained from linear relationship of log i and log v, as shown in Eq (2).

$$\log i = \log a + b \log v \tag{6}$$

By plotting log i vs log v, b values of cathodic and anodic peaks could be obtained. It is generally accepted that the b value reflects energy storage features of electrode materials. There are two well-defined conditions: $b = 0.5$ and $b = 1.0$. In the case of $b = 0.5$, electrochemical energy was stored via a faradaic intercalation process. In the case of $b = 1.0$, current exhibits a capacitive response [65]. As shown in Fig. S3b, b values of cathodic and anodic peaks in NiO were calculated to be 0.514 and 0.408, indicating a diffusion dominated Li^+ ion storage. The b values of Co3O4 were 0.619 and 0.644 in cathodic and anodic scan (See Fig. S3e). Both the b value of cathodic and anodic peaks fall in a range between 0.5 and 1.0, implying Li^+ ions storage in Co3O4 is mainly controlled by pseudocapacitive process. Unidentical Li^+ ions storage kinetics may be a key reason for the difference between cycling stability and rate performance of NiO and Co_3O_4 anode. As pseudocapacitive Li^+ ions storage mainly took place on surface region of electrode, it has higher rate performance [67]. Kinetic analysis revealed that pseudocapacitive plays a dominant role in lithium storage of Co_3O_4.

In order to figure out the contribution ratio of capacitance, relationship in Eq (1) was further divided into two parts corresponding to capacitive (k_1v) and diffusion-controlled effects ($k_2v^{1/2}$), as follows.

$$i = k_1 + k_2v^{1/2} \tag{7}$$

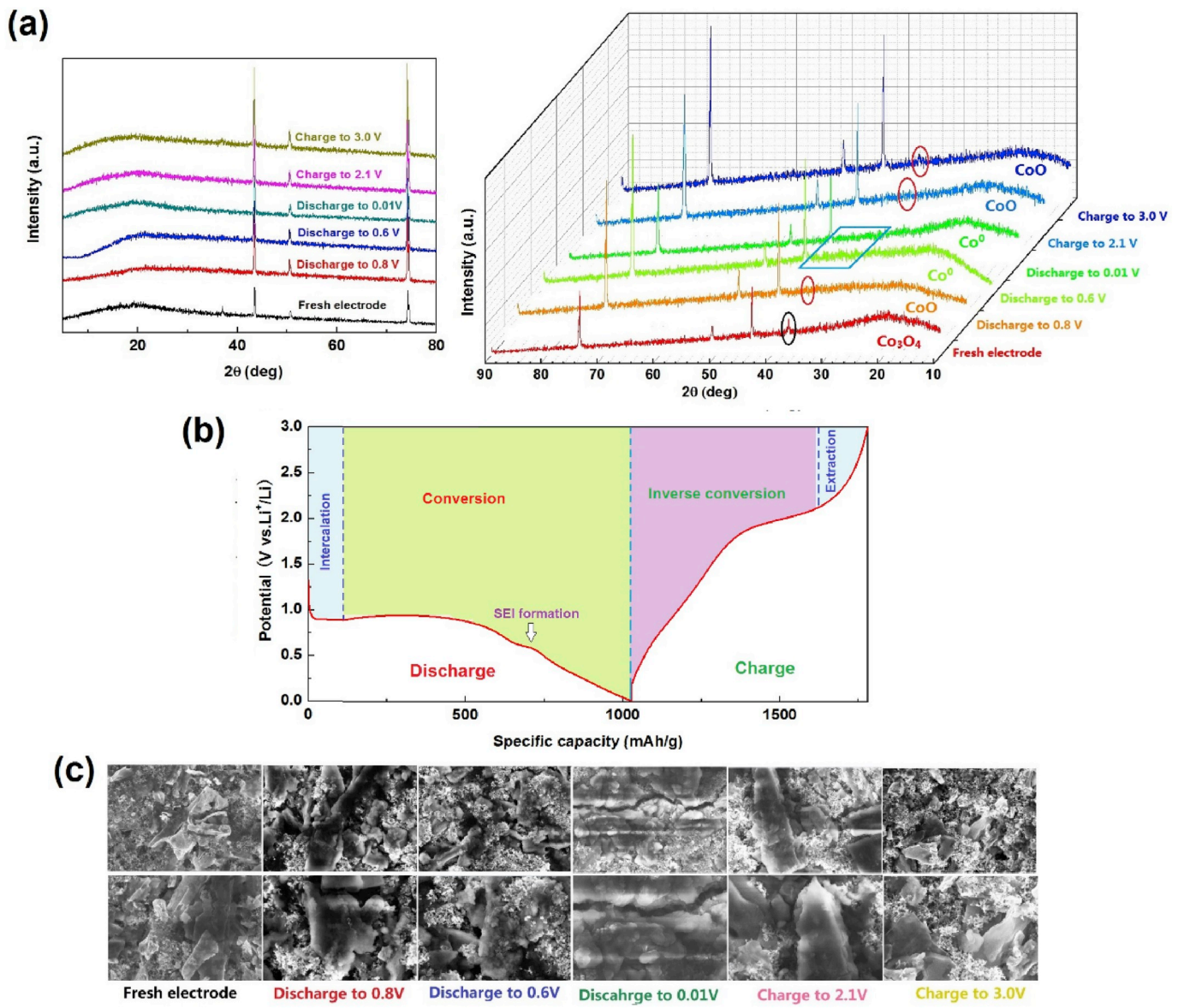

Fig. 6. Ex-situ XRD patterns and FE-SEM images of Co_3O_4 anode at different charge/discharge states during the initial cycle. (a) Ex-situ XRD patterns; (b) Energy storage mechanisms of Co_3O_4 at different charge/discharge states; (c) Ex-situ FE-SEM images at different states.

where k_1 and k_2 are constants for a given potential.

In order to simplify analytical process, Eq (3) was rearranged as follows.

$$i(V) \Big/ v^{1/2} = k_1 v^{1/2} + k_2 \quad (8)$$

By plotting $i/v^{1/2}$ vs $v^{1/2}$, k_1 is determined as slope, and k_2 is determined as intercept; thus capacitive and diffusion contributions can be obtained [66]. As scan rate gradually levelled up, an increasing capacitive contribution ratio could be observed in both NiO and Co_3O_4. In consistence with the kinetic analysis result, Li^+ ions storage in the NiO is dominated by diffusion controlled process. By contrast, the pseudocapacitance plays a dominant role in Li^+ ion storage in the Co_3O_4. Pseudocapacitive process could contribute a capacity as high as 81.83% of the overall capacity at a high scan rate of 1.50 mV s^{-1}. Thus, superior performance of the Co_3O_4 anode may arise from these following reasons: (1) larger pore size between adjacent units could effectively buffer volume expansion during lithiation; (2) higher oxygen vacancy density could facilitate the charge transfer and provide more active sites for pseudocapacitive Li^+ ions storage [43].

As previously reported, conversion mechanism of spinel Co_3O_4 has been proposed [68,69]. Although some oxygen vacancies were introduced into the Co_3O_4 crystal structure, the overall spinel skeleton remained unchanged. Thus, it is anticipated that oxygen-defective Co_3O_4 anode should have analogous lithiation/delithiation process to those defect-free Co_3O_4. Hence, conversion mechanism of the Co_3O_4 was confirmed by ex-situ XRD and ex-situ FE-SEM. The detailed ex-situ XRD patterns and FE-SEM images were shown in Fig. 6.

As shown in Fig. 6a, ex-situ XRD patterns of the Co_3O_4 anode at different charge/discharge states were collected. An obvious diffraction

Table 2
Electrochemical lithiation/delithiation process of Co_3O_4.

Process	Chemical equation	Mechanism
Discharge S_1	$Co_3O_4 + xLi^+ + xe^- \rightarrow Li_xCo_3O_4$	Intercalation
S_2	$Li_xCo_3O_4 + (2\text{-}x)Li^+ + (2\text{-}x)e^- \rightarrow 3CoO + Li_2O$ $CoO + 2Li^+ + 2e^- \rightarrow Co + Li_2O$	Conversion
Charge S_3	$Co + Li_2O \rightarrow Li_xCoO + (2\text{-}x)Li^+ + (2\text{-}x)e^-$	Inverse conversion
S_4	$Li_xCoO \rightarrow CoO + xLi^+ + xe^-$	De-intercalation

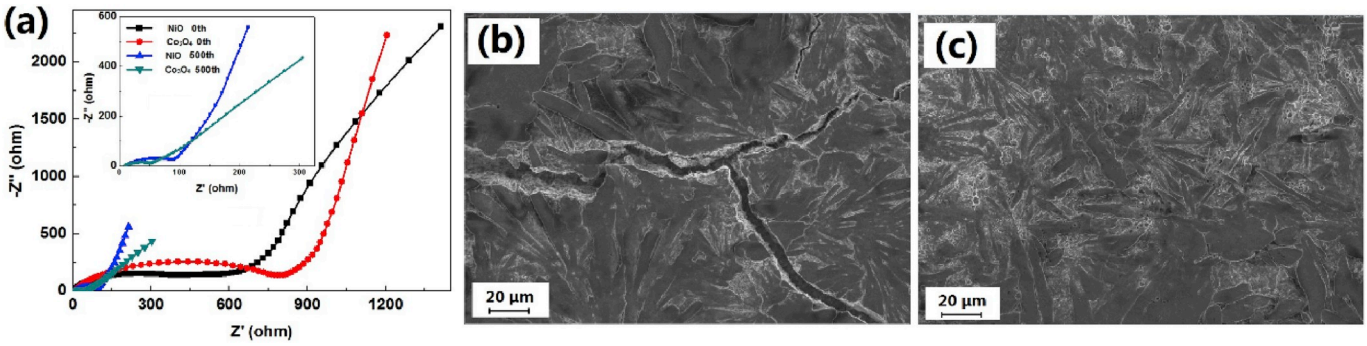

Fig. 7. Nyquist plots and FE-SEM images of the NiO and Co_3O_4 after 500 cycles. (a) Nyquist plots measured with a 10 mV amplitude over a frequency range of 100 kHz and 0.01 Hz before and after 500 cycles; (b) FE-SEM image of NiO after 500 cycles; (c) FE-SEM image of Co_3O_4 after 500 cycles.

peak related to cubic spinel Co_3O_4 (marked in black cycle) was observed on the fresh electrode. Pristine Co_3O_4 is reduced to CoO when the electrode was discharged to 0.8 V, with weaker characteristic peak shifted to higher 2θ value. As the lithiation proceed to 0.6 V, diffraction peak related to CoO disappeared, while the peak related to metallic Co^0 emerged. When the electrode was further lithiated to 0.01 V, the diffraction pattern showed no obvious change. Diffraction peak related to CoO re-emerged as electrode was charged back to 2.1 V, indicating metallic Co is oxidized into CoO. When the electrode was further delithiated to 3.0 V, no signal related to Co_3O_4 could be detected, while diffraction peak of CoO remain unchanged. This phenomenon matched with other previous reports, where reduction of Co_3O_4 to metallic Co is irreversible, while conversion between metallic Co and CoO is reversible [68,69]. Thus, according to analysis of ex-situ XRD and previous reports, a four-stage lithiation/delithion reaction mechanism was put forward. As illustrated in Fig. 6b, certain amount of Li^+ ions were intercalated into Co_3O_4 in the first stage, forming $Li_xCo_3O_4$ phase with partially disordered rocksalt structure [70]. The volume change of electrode material is ignorable in this stage due to its intercalation nature. As more Li^+ ion were inserted into the electrode, incoming Li^+ ions would react with $Li_xCo_3O_4$ via conversion mechanism to generate CoO and Li_2O. The CoO would be further reduced to metallic Co at a lower discharge potential. The majority of lithium storage capacity and volume expansion originate from the second stage of conversion reaction. The subsequent delithiation would proceed via an inverse conversion and deintercalation mechanism, during which metallic Co would be oxidized into CoO. Thus, a detailed four-stage lithiation/delithiation mechanism of Co_3O_4 was presented in Table 2.

Morphology evolution of the Co_3O_4 electrode during the first lithiation delithiation cycle was observed by ex-situ FE-SEM. The enlarged ex-situ FE-SEM images could be found in Fig. S5. As shown in Fig. 6c, sheet-like Co_3O_4 could easily be observed on the fresh electrode. Some aggregates could be found when the electrode was discharged to 0.8 V. Surface of nanosheets were covered with a layer of transparent SEI thin film. More aggregates and thicker SEI film could be found as the electrode was further lithiated to 0.6 V. When the electrode was discharged to 0.01 V, an obvious crack appeared which might originate from the lithiation-induced stress. Although the Co_3O_4 electrode experienced large volume expansion, the majority of nanosheets did not break down. During the subsequent charge process, these lithiation-induce cracks completely disappeared. Sheet-like morphology was found to be recovered when the electrode was charged to 2.1 V. Some residual SEI thin film could still be observed on the surface of active species. When charged to 3.0 V, morphology of the electrode could almost completely recovered to its pristine state. Reversible morphology evolution revealed by ex-situ FE-SEM confirmed considerable stability of the Co_3O_4 anode.

Previous reports have confirmed that the resistance and morphology of electrode would change a lot after repeated charge-discharge cycles [20]. Thus, in order to investigate the variations on resistance, corresponding Nyquist plots of NiO and Co_3O_4 anode were collected by AC-EIS. Typically, Nyquist plots consisted of a semicircle in the high-to-middle frequency region and a slope line in low-frequency region [43]. The high frequency semicircle (R_f) is ascribed to SEI layer resistance and dielectric relaxation capacitance. The middle frequency semicircle (R_{ct}) is related to charger transfer resistance and double-layer capacitance. The slope line at low frequency represents Li^+ ions diffusion process in electrode materials. Fig. 7 shows the Nyquist plots and FE-SEM images of the NiO and Co_3O_4 after 500 cycles.

As shown in Fig. 7a, fresh NiO anode showed a larger semicircle (R_f) than Co_3O_4 at high frequency region, indicating a higher SEI-related resistance. This is in well consistent with the result of GCD test, in which the NiO anode had a lower initial Coulombic efficiency. Relative small particle size in NiO may trigger more side reaction between NiO and the electrolyte, resulting in an excess formation of SEI film. A higher instinct electrical conductivity of Co_3O_4 may also lead to a lower R_{ct} than the NiO anode. As revealed by a steeper slope line in low frequency region, the Co_3O_4 is also found to have a lower interfacial diffusion resistance than NiO. Comparing with fresh electrodes, both the NiO and Co_3O_4 had significantly lower resistance after a 500-cycle GCD test. Sharp decrease in resistance could be attributed to the gradual activation of electrode during repeated charge-discharge cycles [16]. Due to improved interfacial contact, value of R_{ct} in NiO and Co3O4 is much smaller than their pristine state. Both NiO and Co_3O_4 could maintain their original morphology feature after 500 cycles. Clear boundaries between active species and additive agents could not be observed any more at the end of cycling test. Disappearance of these boundaries could also confirm improvement of interfacial contact, which matches with the result revealed by EIS spectra. Some cracks could be observed on the NiO, which may originate from stress accumulation during repeated cycles. The Co_3O_4 has a smoother surface than NiO, indicating a higher stability.

4. Conclusion

In conclusion, oxygen-defective Co_3O_4 with attractive electrochemical performance was successfully prepared via a MOF-derived strategy. Ex-situ XRD revealed reversible conversion between metallic Co^0 and CoO during the charge-discharge process. Reversible morphology evolution was confirmed by ex-situ FE-SEM. The lithium storage capacity of NiO was dominated by a diffusion controlled process, while the lithium ions storage in Co_3O_4 was governed by a pseudocapacitance controlled process. The oxygen-defective Co_3O_4 demonstrated as a promising anode for LIBs.

Acknowledgement

This work was supported by the New Century Talent Support Plan of the Ministry of Education of China [Grant No. 2007NCET-07-0723], and

the National Natural Science Foundation of China [Grant No. 60936003].

Appendix A. Supplementary data

Supplementary data to this article can be found online at https://doi.org/10.1016/j.jpowsour.2019.227026.

References

[1] J. Liu, Addressing the grand challenges in energy storage, Adv. Funct. Mater. 23 (2013) 924–928.
[2] S. Chu, A. Majumdar, Opportunities and challenges for a sustainable energy future, Nature 488 (2012) 294–303.
[3] B. Dunn, H. Kamath, J.M. Tarascon, Electrical energy storage for the grid: a battery of choices, Science 334 (2011) 928–935.
[4] J.B. Goodenough, K.S. Park, The Li-ion rechargeable battery: a perspective, J. Am. Chem. Soc. 135 (2013) 1167–1176.
[5] X. Su, Q. Wu, J. Li, X. Xiao, A. Lott, W. Lu, B.W. Sheldon, J. Wu, Silicon-based nanomaterials for lithium-ion batteries: a review, Adv. Energy Mater. 4 (2014), 1300882.
[6] M.S. Ko, S.J. Chae, J.Y. Ma, N.H. Kim, H.W. Lee, Y. Cui, J. Cho, Scalable synthesis of silicon nanolayer embedded graphite for high-energy lithium-ion batteries, Nat. Energy 1 (2016), 16113.
[7] Y.Y. Liu, G.M. Zhou, K. Liu, Y. Cui, Design of complex nanomaterials for energy storage: past success and future opportunity, Acc. Chem. Res. 50 (2017) 2895–2905.
[8] N. Liu, H. Wu, M.T. Mc Dowell, Y. Yao, C. Wang, Y. Cui, A yolk-shell design for stabilized and scalable Li-ion battery alloy anodes, Nano Lett. 12 (2012) 3315–3321.
[9] Z. Lu, N. Liu, H.W. Lee, J. Zhao, W. Li, Y. Li, Y. Cui, Nonfilling carbon coating of porous silicon micrometer-sized particles for high-performance lithium battery anodes, ACS Nano 9 (2015) 2540–2547.
[10] C.Q. Wu, J. Lin, R.X. Chu, J. Zheng, Y.L. Chen, J. Zhang, H. Guo, Reduced graphene oxide as a dual-functional enhancer wrapped over silicon/porous carbon nanofibers for high-performance lithium-ion battery anodes, J. Mater. Sci. 52 (2017), 7984−7496.
[11] S.H. Yu, X.R. Feng, N. Zhang, J. Seok, H.D. Abruna, Understanding conversion-type electrodes for lithium rechargeable batteries, Accounts Chem. Res. 51 (2018) 273–281.
[12] Y. Zhao, X.F. Li, B. Yan, D.B. Xiong, D.J. Li, S. Lawes, X.L. Sun, Recent developments and understanding of novel mixed transition metal oxides as anodes in lithium ion batteries, Adv. Energy Mater. 6 (2016), 1502175.
[13] S.H. Yu, S.H. Lee, D.J. Lee, Y.E. Sung, T. Hyeon, Conversion reaction-based oxide nanomaterials for lithium ion battery anodes, Small 12 (2016) 2146–2172.
[14] F.F. Wu, J. Bai, J.K. Fenf, S.L. Xiong, Porous mixed metal oxides: design, formation mechanism, and application in lithium ion batteries, Nanoscale 7 (2015) 17211–17230.
[15] V. Soundharrajan, B. Sambandam, J.J. Song, S.J. Kim, J.G. Jo, P.T. Duong, S. H. Kim, V. Mathew, J. Kim, Metal organic framework-combustion: a one-pot strategy to NiO nanoparticles with excellent anode properties for lithium ion batteries, J. Energy Chem. 27 (2018) 300–305.
[16] K. Jang, D.K. Hwang, F.M. Auxilia, J. Jang, H. Song, B.Y. Oh, Y. Kim, J. Nam, J. W. Park, S. Jeong, S.S. Lee, S. Choi, I.S. Lim, W.B. Kim, J.M. Myoung, M.H. Ham, Sub-10-nm Co_3O_4 nanoparticles/graphene composites as high performance anodes for lithium storage, Chem. Eng. J. 309 (2018) 15–21.
[17] T.V. Thi, A.K. Rai, J. Gim, J. Kim, High performance of Co-doped NiO nanoparticle anode material for rechargeable lithium ion batteries, J. Power Source 292 (2015) 23–30.
[18] J.Y. Chen, X.F. Wu, Q.Q. Tan, Y.F. Chen, Designed synthesis of ultrafine NiO nanocrystals bonded on a three dimensional graphene framework for high-capacity lithium-ion batteries, New J. Chem. 42 (2018) 9901–9910.
[19] C.Y. Ding, W.W. Zhou, X.Y. Wang, B. Shi, D. Wang, P.Y. Zhou, G.W. Wen, Hybrid aerogel-derived carbon/porous reduced graphene oxide dual-functionalized NiO for high-performance lithium storage, Chem. Eng. J. 332 (2018) 479–485.
[20] Z.Y. Fan, J. Liang, W. Yu, S.J. Ding, S.D. Cheng, G. Yang, Y.L. Wang, Y.X. Xi, K. Xi, R.V. Kumar, Ultrathin NiO nanosheets anchored on a highly ordered nanostructured carbon as an enhanced anode for lithium ion batteries, Nano Energy 16 (2015) 152–162.
[21] Q. Luo, M.Y. Peng, X.P. Sun, A.M. Asiri, Hierarchical nickel oxide nanosheet@ nanowire arrays on nickel foam: an efficient 3D electrode for methanol electrooxidation, Catal. Sci. Technol. 6 (2016) 1157–1161.
[22] Q.M. Gan, H.N. He, K.M. Zhao, Z. He, S.Q. Liu, Morphology-dependent electrochemical performance of Ni-1,3,5-benzenetricarboxylate metal-organic frameworks as an anode material for Li-ion batteries, J. Colloid Interface Sci. 530 (2018) 127–136.
[23] N. Hu, Z. Tang, P.K. Shen, Hierarchical NiO nanobelt film array as an anode for lithium ion batteries with enhanced electrochemical performance, RSC Adv. 8 (2018) 26589–26895.
[24] S.K. Park, J.H. Choi, Y.C. Kang, Unique hollow NiO nanooctahedrons fabricated through the Kirkendall effect as anodes for enhanced lithium-ion storage, Chem. Eng. J. 354 (2018) 327–334.
[25] J.Y. Chen, X.F. Wu, Y. Liu, Y. Gong, P.F. Wang, W.H. Li, S.P. Mo, Q.Q. Tan, Y. F. Chen, Hierarchically-structured hollow NiO nanospheres nitrogen-doped graphene hybrid with superior capacity retention and enhanced rate capability for lithium-ion batteries, Appl. Surf. Sci. 425 (2017) 461–469.
[26] J.M. Xu, H.B. Tang, T.T. Xu, D. Wu, Z.F. Shi, Y.T. Tian, X.J. Li, Porous Ni O hollow quasi-nanospheres derived from a new metal-organic framework template as high-performance anode materials for lithium ion batteries, Ionics 23 (2017) 3273–3280.
[27] J.B. Li, D. Yan, S.J. Hou, T. Lu, Y.F. Yao, H.C. Chua Daniel, L.K. Pan, Metal-organic frameworks derived yolk-shell ZnO/NiO microspheres as high-performance anode materials for lithium-ion batteries, Chem. Eng. J. 335 (2018) 579–589.
[28] X.J. Yin, H.Q. Chen, C.W. Zhi, W.W. Sun, L.P. Lv, Y. Wang, Functionalized graphene quantum dot modification of yolk–shell NiO microspheres for superior lithium storage, Small 14 (2018), 1800589.
[29] Y.L. Ma, X. Wang, X.D. Sun, T. Gao, Y.L. Liu, L. Zhang, Z.A. Huo QS Qiao, Core–shell structured hierarchically porous NiO microspheres with enhanced electrocatalytic activity for oxygen evolution reaction, Inorg. Chem. Front. 5 (2018) 1199–1206.
[30] H.J. Wu, Y.Q. Wang, C.H. Zheng, J.M. Zhu, G.L. Wu, X.H. Li, Multi-shelled NiO hollow spheres: easy hydrothermal synthesis and lithium storage performances, J. Alloy. Comp. 685 (2016) 8–14.
[31] S.J. Hao, B.W. Zhang, S. Ball, B. Hu, J.S. Wu, Y.Z. Huang, Porous and hollow NiO microspheres for high capacity and long-life anode materials of Li-ion batteries, Mater. Des. 92 (2016) 160–165.
[32] B.B. Chang, Z.Y. Gu, Y.Z. Guo, Z.K. Li, B.C. Yang, Glucose-assisted synthesis of Co_3O_4 nanostructure with controllable morphologies from nanosheets to nanowires, J. Alloy. Comp. 676 (2016) 26–36.
[33] T. Zhu, Y. Xie, G.X. Zhang, Z.N. He, Y.S. Lu, H.B. Guo, C. Lin, Y.G. Chen, Magnetic-field-assisted synthesis of Co_3O_4 nanoneedles with superior electrochemical capacitance, J. Nanoparticle Res. 17 (2015) 484–493.
[34] K. Jang, D.K. Hwang, F.M. Auxilia, J. Jang, H. Song, B.Y. Oh, Y. Kim, J. Nam, J. W. Park, S. Jeong, S.S. Lee, S. Choi, I.S. Lim, W.B. Kim, J.M. Myoung, M.H. Ham, Sub-10-nm Co_3O_4 nanoparticles/graphene composites as high performance anodes for lithium storage, Chem. Eng. J. 309 (2018) 15–21.
[35] X.Y. Deng, S. Zhu, F. He, E.Z. Liu, C.N. He, C.S. Shi, Q.Y. Li, J.J. Li, L.Y. Ma, N. Q. Zhao, Three-dimensionally hierarchical Co_3O_4/Carbon composites with high pseudo-capacitance contribution for enhancing lithium storage, Electrochim. Acta 283 (2018) 1269–1276.
[36] X. Li, X.D. Tian, T. Yang, Y. Song, Z.J. Liu, Hierarchically multiporous carbon nanotube/Co_3O_4 composite as an anode material for high performance lithium-ion batteries, Chem. Eur J. 24 (2018) 14477–14483.
[37] H.B. Geng, Y.Y. Guo, X.G. Ding, H.W. Wang, Y.F. Zhang, X.L. Wu, J. Jiang, J. W. Zheng, Y.G. Yang, H.W. Gu, Porous cubes constructed by cobalt oxide nanocrystals with graphene sheet coatings for enhanced lithium storage properties, Nanoscale 8 (2016) 7688–7694.
[38] J.B. Li, D. Yan, S.J. Hou, T. Lu, Y.F. Yao, L.K. Pan, Metal-organic frameworks converted flower-like hybrid with Co_3O_4 nanoparticles decorated on nitrogen-doped carbon sheets for boosted lithium storage performance, Chem. Eng. J. 354 (2018) 172–181.
[39] T. Kesavan, S. Boopathi, M. Kundu, G. Maduraiveeran, M. Sasidharan, Morphology-dependent electrochemical performance of spinel cobalt oxide nanomaterials towards lithium-ion batteries, Electrochim. Acta 283 (2018) 1668–1678.
[40] A. Li, M. Zhong, W. Shuang, C.P. Wang, J. Liu, Z. Chang, X.H. Bu, Facile synthesis of Co_3O_4 nanosheets from MOF nanoplates for high performance anodes of lithium-ion batteries, Inorg. Chem. Front. 5 (2018) 1602–1608.
[41] Y.H. Dou, T. Liao, Z.Q. Ma, D.L. Tian, Q.N. Liu, F. Xiao, Z.Q. Sun, J.H. Kim, S. X. Dou, Graphene-like holey Co_3O_4 nanosheets as a highly efficient catalyst for oxygen evolution reaction, Nano Energy 30 (2016) 267–275.
[42] K. Wang, Y.L. Cao, J.D. Hu, Y.Z. Li, J. Xie, D.Z. Jia, Solvent-free chemical approach to synthesize various morphological Co_3O_4 for CO oxidation, ACS Appl. Mater. Interfaces 9 (2017) 16128–16137.
[43] R.J. Wei, X.L. Zhou, T.F. Zhou, J.C. Hu, J.C. Ho, Co_3O_4 nanosheets with in-plane pores and highly active {112} exposed facets for high performance lithium storage, J. Phys. Chem. C 121 (2017) 19002–19009.
[44] J.X. Wang, C. Wang, M.M. Zhen, Template-free synthesis of multifunctional Co_3O_4 nanotubes as excellent performance electrode materials for superior energy storage, Chem. Eng. J. 356 (2019) 1–10.
[45] C.S. Yan, C. Chen, X. Zhou, J.X. Sun, C.D. Lv, Template-based engineering of carbon-doped Co_3O_4 hollow nanofibers as anode materials for lithium-ion batteries, Adv. Funct. Mater. 26 (2016) 1428–1436.
[46] Y.M. Chen, L. Yu, X.W. Lou, Hierarchical tubular structures composed of Co_3O_4 hollow nanoparticles and carbon nanotubes for lithium storage, Angew. Chem. Int. Ed. 55 (2016) 5990–5993.
[47] A. Numan, N. Duraisamy, F.S. Omar, Y.K. Mahipal, K. Ramesh, S. Ramesh, Enhanced electrochemical performance of cobalt oxide nanocube intercalated reduced graphene oxide for supercapacitor application, RSC Adv. 6 (2016) 34894–34902.
[48] R.B. Wu, X.K. Qian, X.H. Rui, H. Liu, B. Yadian, K. Zhou, J. Wei, Q.Y. Yan, X. Q. Feng, Y. Long, L.Y. Wang, Y.Z. Huang, Zeolitic Imidazolate Framework 67-derived high symmetric porous Co_3O_4 hollow dodecahedra with highly enhanced lithium storage capability, Small 10 (2014) 1932–1938.
[49] Y.Z. Wu, J.S. Meng, Q. Li, C.J. Niu, X.P. Wang, W. Yang, W. Li, L.Q. Mai, Interface-modulated fabrication of hierarchical yolk–shell Co_3O_4/C dodecahedrons as stable anodes for lithium and sodium storage, Nano Res. 10 (2017) 2364–2376.

[50] Z.Z. Liu, W.W. Zhou, S.S. Wang, W. Du, H.L. Zhang, C.Y. Ding, Y. Du, L.J. Zhu, Facile synthesis of homogeneous core-shell Co_3O_4 meso-porous nanospheres as high performance electrode materials for supercapacitor, J. Alloy. Comp. 774 (2019) 137–144.
[51] T. Xie, J. Min, J. Liu, J.J. Chen, D.J. Fu, R.Z. Zhang, K.J. Zhu, M. Lei, Synthesis of mesoporous Co_3O_4 nanosheet-assembled hollow spheres towards efficient electrocatalytic oxygen evolution, J. Alloy. Comp. 754 (2018) 72–77.
[52] J.Y. Wang, N.L. Yang, H.J. Tang, Z.H. Dong, Q. Jin, M. Yang, D. Kisailus, H.J. Zhao, Z.Y. Tang, D. Wang, Accurate control of multishelled Co_3O_4 hollow microspheres as high-performance anode materials in lithium ion batteries, Angew. Chem. 125 (2013) 6545–6548.
[53] Y.N. Men, X.C. Liu, F.L. Yang, F.S. Ke, G.Z. Cheng, W. Luo, Carbon encapsulated hollow Co_3O_4 composites derived from reduced graphene oxide wrapped metal organic frameworks with enhanced lithium storage and water oxidation properties, Inorg. Chem. 57 (2018) 10649–10655.
[54] R. Zhao, Z.B. Liang, R.Q. Zuo, Q. Xu, Metal organic frameworks for batteries, Joule 2 (2018) 2235–2259.
[55] G.J. Wei, Z. Zhou, X.X. Zhao, W.Q. Zhang, C.H. An, Ultrathin metal organic framework nanosheet-derived ultrathin Co_3O_4 nanomeshes with robust oxygen evolving performance and asymmetric supercapacitors, ACS Appl. Mater. Interfaces 10 (2018) 23721–23730.
[56] Q. Wang, Y.L. Cao, J.D. Hu, Y.Z. Li, J. Xie, D.Z. Jia, Solvent-free chemical approach to synthesize various morphological Co_3O_4 for CO oxidation, ACS Appl. Mater. Interfaces 9 (2017) 16128–16137.
[57] D.L. Liu, C. Zhang, Y.F. Yu, Y.M. Shi, Y. Yu, Z.Q. Niu, B. Zhang, Hydrogen evolution activity enhancement by tuning the oxygen vacancies in self-supported mesoporous spinel oxide nanowire arrays, Nano Res. 11 (2) (2018) 603–613.
[58] J. Zhang, R.X. Chu, Y.L. Chen, H. Jiang, Y. Zhang, N.M. Huang, H. Guo, Electrodeposited binder-free $NiCo_2O_4$ @carbon nanofiber as a high performance anode for lithium ion batteries, Nanotechnology 29 (2018), 125401.
[59] Q.M. Su, J. Zhang, Y.S. Wu, G.H. Du, Revealing the electrochemical conversion mechanism of porous Co_3O_4 nanoplates in lithium ion battery by in situ transmission electron microscopy, Nano Energy 9 (2014) 264–272.
[60] V. Pralong, J.B. Leriche, B. Beaudoin, E. Naudin, Tarascon JM. Morcrette, Electrochemical study of nanometer Co_3O_4, Co, $CoSb_3$ and Sb thin films toward lithium, Solid State Ion. 166 (2004) 295–305.
[61] R. Dedryvere, S. Laruelle, S. Grugeon, P. Poizot, D. Gonbeau, J.M. Tarascon, Contribution of X-ray photoelectron spectroscopy to the study of the electrochemical reactivity of CoO toward lithium, Chem. Mater. 16 (2004) 1056–1061.
[62] I. Bouessay, A. Rougier, P. Poizot, J. Moscovici, A. Michalowicz, J.M. Tarascon, Electrochromic degradation in nickel oxide thin film: a self-discharge and dissolution phenomenon, Electrochim. Acta 50 (2005) 3737–3745.
[63] F. Mestre-Aizpurua, S. Laruelle, S. Grugeon, J.M. Tarascon, M.R. Palacın, High temperature lithium cells using conversion oxide electrodes, J. Appl. Electrochem. 40 (2010) 1365–1370.
[64] C.S. Yan, Y. Zhu, Y.T. Li, Z.W. Fang, L.L. Peng, X. Zhou, G. Chen, G.H. Yu, Local built-in electric field enabled in carbon-doped Co_3O_4 nanocrystals for superior lithium-ion storage, Adv. Funct. Mater. 28 (2018), 1705951.
[65] X. Xu, R.S. Zhao, W. Ai, B. Chen, H.F. Du, L.S. Wu, H. Zhang, W. Huang, T. Yu, Controllable design of MoS_2 nanosheets anchored on Nitrogen-doped graphene: toward fast sodium storage by tunable pseudo-capacitance, Adv. Mater. 30 (2018), 1800658.
[66] C. Liao, S.P. Wu, Pseudo-capacitance behavior on Fe_3O_4-pillared SiO_x microsphere wrapped by graphene as high performance anodes for lithium-ion batteries, Chem. Eng. J. 355 (2019) 805–814.
[67] J.H. Han, A. Hirata, J. Du, Y. Ito, T. Fujita, S. Kohara, T. Ina, M.W. Chen, Intercalation pseudo-capacitance of amorphous titanium dioxide@ nano-porous graphene for high-rate and large-capacity energy storage, Nano Energy 49 (2018) 354–362.
[68] P. Ge, C.Y. Zhang, H.S. Hou, B.K. Wu, L. Zhou, S.J. Li, T.J. Wu, J.G. Hu, L.Q. Mai, X. B. Ji, Anions induced evolution of Co_3X_4 (X = O, S, Se) as sodium-ion anodes: the influences of electronic structure, morphology, electrochemical property, Nano Energy 48 (2018) 617–629.
[69] L.L. Luo, J.S. Wu, J.M. Xu, V.P. Dravid, Atomic resolution study of reversible conversion reaction in metal oxide electrodes for lithium-ion battery, ACS Nano 11 (2014) 11560–11566.
[70] Z.P. Yao, S. Kim, M. Aykol, Q.Q. Li, J.S. Wu, J.G. He, C. Wolverton, Revealing the conversion mechanism of transition metal oxide electrodes during lithiation from first-principles, Chem. Mater. 29 (2017) 9011–9022.